Modeling and Design of Passive Shield to Limit EMF Emission and to Minimize Shield Loss in Unipolar Wireless Charging System for EV

Mostak Mohammad, *Student Member, IEEE*, Eshet Tezera Wodajo, *Student Member, IEEE*, Seungdeog Choi, *Senior Member, IEEE*, and Malik E. Elbuluk, *Senior Member, IEEE*

***Abstract*—In this paper, a detailed lumped model of the shield is developed, and an optimization method is proposed to minimize the shield loss while suppressing the emission within the standard limit. The electromagnetic emission in a wireless charging system (WCS) is a serious concern for health and safety, especially for medium- and high-power applications, where strong magnetic field propagates through a large air gap. Usually, a flat aluminum plate is used as a shield to suppress the emission outside the charging area. This field emission increases proportionally with the coil ampere turn; therefore, a much higher shield current is required to suppress the additional emission under the limit set by the International Commission on Non-Ionizing Radiation Protection. In this paper, a novel hybrid shield structure is proposed to limit the electromagnetic field (EMF) emission, as well as to minimize the shield loss. The proposed shielding is evaluated on a laboratory prototype of 7-kW WCS designed for electric vehicle application. The experimental result shows that, while suppressing the EMF under the limit, the shield loss has been reduced by 21% compared to the commonly used aluminum shield.**

***Index Terms*—Electric vehicles (EVs), electromagnetic field (EMF), ferrite core, inductive charging, magnetic shielding, wireless power transfer.**

I. Introduction

WIRELESS charging systems (WCSs) are being investigated for many different applications for the past few decades [1]–[4]. In a typical vehicular WCS, there is one transmitter (Tx) and one receiver (Rx) pad separated by about 100–200 mm air gap. [4]–[6]. Each of these pads is usually made with one or multiple coils, a ferrite core, and an aluminum (Al) shield, as shown in Fig. 1. High frequency ac current through the transmitter coil generates a high frequency magnetic field which propagates through a large air gap to reach the receiver. Therefore, there is a high possibility of magnetic field emission outside the charging region. This emission is quite small for low-power wireless charging applications. However, medium-to-high power applications with a large air-gap generate a considerable level of emission outside the charging area. One of the most promising applications of such power range is automotive charging, where the power can range from several hundred watts to as high as 50 kW. Usually, vehicular charging systems are installed in a commonly accessible area, such as home garage or automobile parking areas. Therefore, when regarding health and safety, it is crucial to limit the electromagnetic field (EMF) emission for this application [7], [8]. In this paper, the EMF emission characteristics and its suppression methods are investigated for a medium-to-high power WCS in automotive applications.

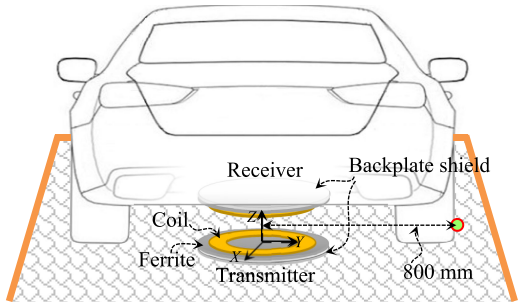

Fig. 1. Typical position and components of the transmitter and receiver pads in a WCS for EV.

For the health and safety purposes, the public and occupational exposure to magnetic field density is set to the maximum of 27 and 100 μT by the International Commission on Non-Ionizing Radiation Protection (ICNIRP) for the frequency range of 3–100 kHz [9]. Therefore, the emission in WCSs is intensively studied and several shielding methods are proposed to keep the electromagnetic emission within the standard limits [10]–[15].

Although the magnetic flux density between the transmitter and the receiver can be very high, the immediate area between the charging pads is not usually publicly exposed since the transmitter and receiver pads are placed under the vehicle. However, the sides of a vehicle can be considered openly exposed and needs to be observed for EMF emission. The minimum distance of these concern areas from the center of a receiver is approximately half of the car width [16], [17], as shown in Fig. 1.

Manuscript received June 20, 2018; revised October 29, 2018 and January 14, 2019; accepted February 21, 2019. Date of publication March 8, 2019; date of current version September 6, 2019. This paper was presented in part at the IEEE Energy Conversion Congress and Exposition in September 2018. Recommended for publication by Associate Editor F. Costa. *(Corresponding author: Mostak Mohammad.)*

The authors are with the University of Akron, Akron, OH 44325 USA (e-mail:

The EMF emission depends on the power level and shielding effectiveness of the charging pads. An aluminum shield is commonly used in the transmitter and receiver to limit the EMF emission for a unipolar WCS. The shield effectively suppresses the EMF emission above the receiver and below the transmitter, but it is comparatively less effective along the sides. Moreover, with the increasing demand for fast vehicle charging, the high-power WCS is becoming a potential solution. However, at high power, the EMF emission at the concern areas tends to increase beyond the ICNIRP limit, and the system requires a highly effective low loss shielding.

Several different active and passive shield designs have been investigated to reduce the EMF emission [11], [12], [17]–[19]. However, the consequent shielding loss is studied limitedly while designing for the EMF suppression. The effectiveness of shielding with material conductivity is studied in [21]. Comparative effectiveness of an aluminum and copper shield is studied in [20] for a circular current carrying loop, where the copper (Cu) shows 1.3 times higher shielding effectiveness than aluminum alloy for up to 100 kHz. The shield characteristics of a resonant active shield are investigated in [22] with effective suppression of EMF, but it has a limited and localized shielding effect, which requires multiple units to suppress EMF at different areas around the vehicle. A shield modeling method is proposed in [23] with an equivalent circuit which can be used only for a specific shield and core combinations. Therefore, there is still a comprehensive study to investigate the shield characteristics and to optimize the shield design for suppressing the EMF while minimizing the shield loss.

In this paper, the characteristics of electromagnetic emission for a unipolar circular pad are studied through an equivalent circuit and finite-element analysis (FEA), especially focusing on the shield current and the shield loss. Finally, a hybrid shield is proposed using an aluminum plate and a thin copper ring, and an optimization method is evaluated to minimize the shield loss while suppressing EMF under the ICNIRP limit of 27 μT at the recommended locations by Society of Automotive Engineers (SAE). The proposed shield modeling is applicable to all unipolar WCS, including the circular and rectangular coils. Compared to the circular coil, in case of rectangular coil, the resulting shield current loop is rectangular, which needs to be considered during the modeling.

In Section II, the characteristics of the EMF are investigated. In Section III, a lumped circuit model is developed for traditional aluminum shielding. In Section IV, a shield optimization method is proposed with an optimization algorithm, its related electric and geometric constraints, and an objective function. Finally, in Section V, the experimental results of EMF suppression and shield loss reduction on a laboratory prototype of a 7-kW WCS are presented.

II. Characteristics of Leakage Field and Shield Loss of Unipolar Pad

The conductive shield provides a barrier for the magnetic flux generated by the transmitter and receiver coil currents and reduces the EMF emission. However, the shield also introduces additional loss in the system due to the high frequency current induced in it. The shielding reduces the effective self and mutual inductance of the transmitter and receiver; hence, an effective and optimized shield is required. In this study, an FEA model is developed, as shown in Fig. 2, to investigate the shielding characteristics focusing on EMF emission and shielding loss. The FEA is done using the Ansys Maxwell *Z*-axis symmetric two-dimensional (2-D) and complete three-dimensional (3-D) model through the eddy analysis. The actual Litz wire has been selected based on the operating frequency and the current requirement allowing the maximum current density of 4 A/mm^2. However, for the simplicity of the FEA, the Litz coil has been modeled in Maxwell as a stranded lumped coil having the same inner, outer radius, and thickness as of the actual coil. The design parameters of the system are given in Table I.

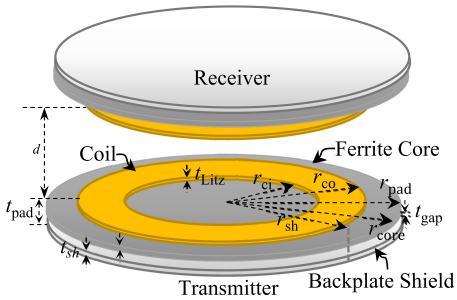

Fig. 2. Traditional circular transmitter and receiver pads with lumped circular coil, ferrite core, and aluminum shield.

TABLE I
Nominal Values of a Traditional Pad

Parameter	Value
Air-gap, d	150 mm
Pad radius, r_{pad}	300 mm
Coil (AWG38/800) inner radius, r_{ci}	150 mm
Coil outer radius, r_{co}	250 mm
Coil thickness, t_{Litz}	4 mm
Core thickness, t_{core}	4 mm
Core radius, r_{core}	300 mm
Shield (Al 6101 alloy) thickness, t_{sh}	4 mm
Coil-core-shield gap, t_{gap}	1 mm
Pad thickness, t_{pad}	14 mm
Coil turn number, N_{tx}, N_{rx}	14, 14
Core model	Feroxxcube-C95
Core relative permeability	3000

A. EMF Emission Considering Misalignment

In a vehicular application, the transmitter and receiver are usually placed around the center of the parking space and the vehicle undercarriage correspondingly, as shown in Fig. 3(a). Therefore, for the commonly accessible region, the EMF observation point is considered at approximately 800 mm away from the center of the vehicle [24]. The corresponding observation point under perfect alignment of the vehicle is shown as P_0 in Fig. 3(b). However, the distance from the transmitter to the observation point changes with misalignment. At a misalignment Δ along the side of the vehicle, the target new observation point P_Δ needs to be defined at (800 mm–Δ) away from the center of

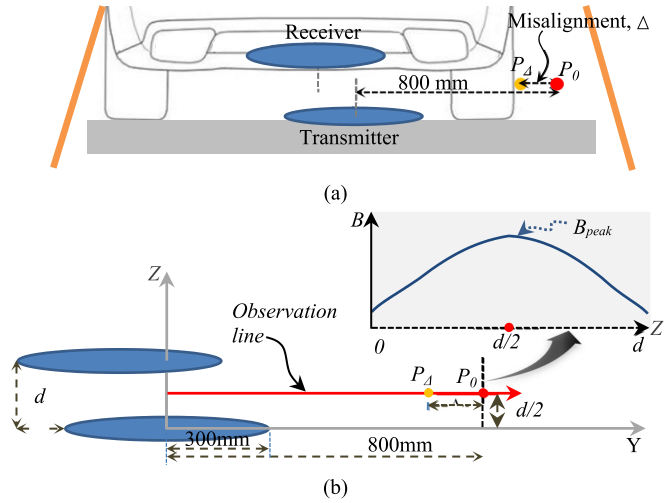

Fig. 3. (a) Typical misalignment scenario for vehicular parking and (b) proposed observation points and observation line considering misalignment.

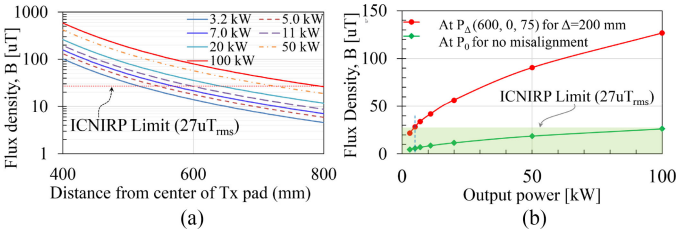

Fig. 4. Variation of flux density (a) along the observation line for perfect alignment, and (b) flux density at observation points P_0 and P_Δ for a traditional shield at different power levels at 85 kHz.

the transmitter as shown in Fig. 3(b). At an observation point, the flux density also varies along the height, as shown in the inset of Fig. 3(b). The maximum flux density is observed at height $d/2$ for an air gap d. Therefore, the new observation point P_Δ is selected at ($y = 800$ mm$-\Delta$, $z = d/2$) point, as shown in Fig. 3(b). Considering 150-mm air gap and the maximum misalignment of 200 mm, the observation point is selected at $y = 600$ mm and $z = 75$ mm.

The EMF emission increases linearly with the current through the transmitter and receiver coils. This phenomenon is investigated in FEA and the resulting flux density along the *observation line* between the transmitter and receiver is shown in Fig. 4(a). The similar flux density variation at the observation point P_0 and P_Δ is shown in Fig. 4(b). It shows that the flux density increases significantly as the distance from the transmitter to the observation point P_Δ reduces with misalignment and the transmitter current increases to maintain the same power at reduced mutual inductance. It exceeds the 27 $\mu\mathrm{T}_{\mathrm{rms}}$ limit for only 5-kW power and 200-mm misalignment. Therefore, in a potentially high-power charging system with higher misalignment tolerance, a more effective shielding method is required to suppress the higher EMF emission.

The variation of the shield loss with the varying power level is shown in Fig. 5. It depicts that the shield loss in the traditional aluminum plate can be quite high, especially at higher current under the misalignment condition. However, the induced current

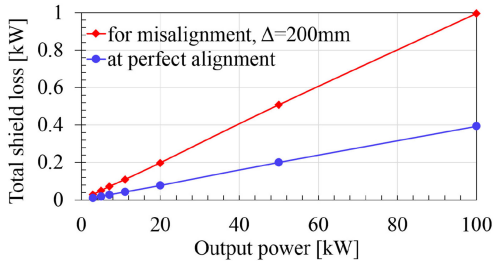

Fig. 5. Total shield loss for different output power for perfectly aligned position with $k = 0.3$ and for $\Delta = 200$ mm with $k = 0.1$.

and loss distribution in the shield is highly localized and concentrated near the outer edge. Therefore, a more effective and efficient shielding method is required to minimize the shield loss while suppressing the EMF emission.

III. Modeling of Shield in WCS

The FEA of the induced shield current and consequent distribution of shield current and shield loss in a 7-kW WCS simulated in Ansys Maxwell are shown in Fig. 6(a)–(c). At resonant point operation, the primary and secondary coil amp turn for the studied 7-kW WCS are shown in Fig. 6(a), where the receiver coil current lags the transmitter coil current by 90°. The consequent shield currents are also shown in Fig. 6(a), where the peak shield current is observed approximately at around 225° relative phase with respect to the primary current. The simulation is done using soft ferrite Feroxxcube-C95 with a relative permeability of 3000 as the core, and the aluminum 1101 alloy as the shield plate [26]. The FEA current distribution shows that approximately 90% of the shield current circulates around at the outer edge of the shield for a nonpolar wireless charging pad. In this region, a significant portion of the magnetic flux exits the core and consequently induces current around the outer edge of the shield. Moreover, since the skin depth of the aluminum is approximately 0.28 mm at 85 kHz frequency, the shield current penetrates only a very thin surface, causing a significant shield loss around the outer radius of the shield, as shown in Fig. 6(c).

A. Equivalent Circuit of Passive Shield

Because the shield current is highly localized and concentrated at the outer edge of the shield, it effectively behaves as a conductor loop with a radius same as shield radius. The magnetic field distribution near the charging system on the *ZY* plane and induced eddy current distribution in the SAE proposed large aluminum shield is shown in Fig. 7(a) and (b). Fig. 7(b) also shows a highly concentrated current density in the back plate and SAE recommended shield, around the outer edge of the core. Therefore, following the current distribution pattern from Figs. 6(b) and 7(b), the effective shield can be modeled as a lumped coil as shown in Fig. 7(c). The equivalent inductance and resistance of this shield loop can be estimated from its outer radius, skin depth, current distribution, and the resistivity of the material. Compared to a stand-alone pad with only Al-back plate shield as in transmitter, the current in the receiver side with SAE recommended shield is shared by both the Al back

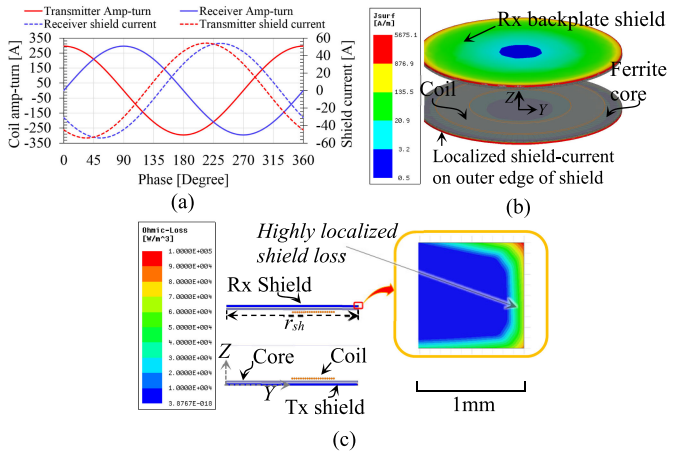

Fig. 6. (a) Amp turn in the coils and consequent induced shield currents, (b) shield current distribution in the back-plate shield of a 3-D FEA model, and (c) consequent shield loss distribution on the radial cross section of a *Z*-axis symmetric 2-D model of a 7-kW circular pad WCS operating at 85 kHz.

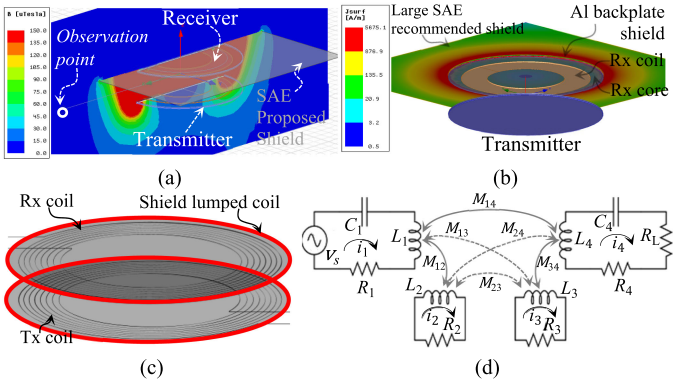

Fig. 7. (a) Peak magnetic field distribution on *ZY* plane and (b) current distribution in the back plate and SAE proposed 800 mm × 800 mm shield, (c) derived lumped model of the shield, and (d) ac equivalent circuit diagram showing equivalent shield components and their interaction with the main coils.

plate and the large aluminum plate, as shown in Fig. 7(b). The equivalent circuit model with the lumped shield coils is given in Fig. 7(d), where each shield is represented as single turn inductor in series with its equivalent resistance. This equivalent circuit has a magnetic coupling with both the coils as well as the other shield. However, the mutual inductance between the transmitter and receiver shield M_{23} is very small and has very little effect on shield characteristics. Therefore, the mutual inductances $M_{14}, M_{12}, M_{13}, M_{24}$, and M_{34} are of main interest for shield design.

B. Equivalent Inductance and Resistance of the Shield

The three most important parameters of this lumped shield coil are the shield inductance, equivalent resistance, and its coupling coefficient with the main coils. Effective inductance of this single loop shield with radius $r_{\rm sh}$ can be expressed as [23], [28], [29]

$$L_{\rm sh} = \mu_{r-{\rm eff}}\,\mu_0 r_{\rm sh}\left(\ln\left(\frac{8r_{\rm sh}}{r_w}\right) - 2\right) \tag{1}$$

where r_w is the radius of equivalent circular wire carrying uniform current on its skin, and $\mu_{r-{\rm eff}}$ is the effective relative permeability considering the presence of core. Due to the complex geometry, it is extremely difficult to analytically solve for the shield inductance. The shield current path is partially surrounded by the core, conductor, and air. The effective permeability of the shield can be estimated as the ratio of the shield inductance to the inductance of a single-loop air-core inductor with the same radius as

$$\mu_{r-{\rm eff}} = \frac{L_{\rm sh}}{L_{\rm loop-in-air}} \tag{2}$$

where the $L_{\rm loop-in-air}$ is the inductance of a circular conductor loop in the air with the same size as lumped shield loop, which can be calculated both analytically and through FEA; it can be also measured directly. On the other hand, the effective shield inductance, $L_{\rm sh}$ is very complex to calculate analytically due to its complex nonlinear geometry partially covered by air and ferrite. However, it can be estimated through FEA. The FEA-based analysis shows a variation of $\mu_{r-{\rm eff}}$ in the range of 1.2–1.3 for different relative geometry of core and shield.

The effective resistance of the shield is mainly determined by its surface current distribution and the skin depth. The skin depth of a conductor can be given as follows [27]:

$$\delta = \sqrt{\frac{\rho}{\pi\mu f}} \tag{3}$$

where δ and ρ are the skin depth and resistivity of the shield material, respectively. At 85 kHz, the skin depth of aluminum is 0.28 mm and skin depth of copper is 0.22 mm. The effective shield resistance considering this high frequency skin effect can be represented as

$$R_{\rm sh} = \frac{\rho l_{\rm eff}}{A_{\rm eff}} \tag{4}$$

where $A_{\rm eff}$ is the equivalent conducting cross-sectional area, and $l_{\rm eff}$ is the equivalent conducting-path distance of the shield current. As shown in Figs. 6(b) and 7(a), most of the shield current is concentrated around the outer edge of the core; therefore, the equivalent length of shield current path is $l_{\rm eff} \approx 2\pi r_{\rm sh} \approx 2\pi r_{\rm core}$. On the other hand, the effective cross-sectional area of the current path is proportional to the skin depth, which can be expressed as $A_{\rm eff} \propto \delta$. Thus, the dependence of the equivalent shield resistance from (4) can be derived as

$$R_{\rm sh} \propto \sqrt{\rho f \mu}. \tag{5}$$

According to the SAE technical recommendation J2954, the operating frequency of the WCS for light-duty automotive application is set to 81.3–90 kHz [24]. The relative permeability of the typically used shield materials, copper, aluminum, etc., are very similar and close to unity. Therefore, for typically used shield materials, the shield resistance varies as $R_{\rm sh} \propto \sqrt{\rho}$. Hence, the ratio of the effective shield resistance of copper and aluminum is approximately 0.79, which indicates that appropriate use of copper can reduce the shield loss. Therefore, in Section IV-A, a shield design is proposed with a copper ring around the aluminum back plate to reduce the shield loss.

C. Shield Current Characteristics

The inductance matrix of the equivalent circuit shown in Fig. 7(b) can be represented as

$$\begin{bmatrix} 1 & k_{12} & k_{13} & k_{14} \\ k_{12} & 1 & k_{23} & k_{24} \\ k_{13} & k_{23} & 1 & k_{34} \\ k_{14} & k_{24} & k_{34} & 1 \end{bmatrix} \begin{bmatrix} L_1 \\ L_2 \\ L_3 \\ L_4 \end{bmatrix} \tag{6}$$

where k_{ij} is the coupling coefficient between i_{th} and j_{th} coil as shown in Fig. 7(b). The mutual inductance between the primary coil and its shield M_{12} and between the secondary coil and its shield M_{34} are negative; hence, $k_{12} < 0, k_{34} < 0$. For a typical EV charging application, $k_{14} > |k_{12}| > k_{13} > k_{23}$ and the equivalent loop inductance of the shield, L_2 and L_3 are also very small. The inductance matrix of the studied 7-kW system extracted from its 3-D FEA simulation under the parameter settings given in Table I is shown as follows:

$$L = \begin{bmatrix} 1 & -0.17 & 0.11 & 0.32 \\ -0.17 & 1 & 0.08 & 0.11 \\ 0.11 & 0.08 & 1 & -0.17 \\ 0.32 & 0.11 & -0.17 & 1 \end{bmatrix} \begin{bmatrix} 190 \\ 1.45 \\ 1.45 \\ 190 \end{bmatrix} \mu\text{H}. \tag{7}$$

It shows that the shield-to-shield mutual inductance M_{23} is very small and can be ignored with the following assumption:

$$M_{23} = k_{23}\sqrt{L_2 L_3} \approx 0. \tag{8}$$

Both shield currents can be considered as uncoupled from each other and the current–voltage relation of the shield and coil currents can be represented in the following matrix form:

$$\begin{bmatrix} v_s \\ 0 \\ 0 \\ 0 \end{bmatrix} = \begin{bmatrix} Z_{11} & -j\omega M_{12} & -j\omega M_{13} & -j\omega M_{14} \\ -j\omega M_{12} & Z_{22} & 0 & -j\omega M_{24} \\ -j\omega M_{13} & 0 & Z_{33} & -j\omega M_{34} \\ -j\omega M_{14} & -j\omega M_{24} & -j\omega M_{34} & Z_{44} \end{bmatrix} \begin{bmatrix} i_1 \\ i_2 \\ i_3 \\ i_4 \end{bmatrix} \tag{9}$$

where Z_{11}, Z_{22}, Z_{33}, and Z_{44} are given as

$$\begin{aligned} Z_{11} &= R_1 + j\omega L_1 + 1/j\omega C_1 \\ Z_{22} &= R_2 + j\omega L_2 \\ Z_{33} &= R_3 + j\omega L_3 \\ Z_{44} &= R_4 + R_L + j\omega L_4 + 1/j\omega C_4. \end{aligned} \tag{10}$$

Both the coil and core equivalent resistances are included in R_1 and R_4. Based on the assumption in (7), the shield currents i_2 and i_3 can be derived from (9) as

$$i_2 = \frac{1}{Z_{22}}(j\omega M_{12} i_1 + j\omega M_{24} i_4) \tag{11}$$

$$i_3 = \frac{1}{Z_{33}}(j\omega M_{13} i_1 + j\omega M_{34} i_4) \tag{12}$$

which shows that both the transmitter and receiver shield currents are dependent only on the primary and secondary coil current. Therefore, putting the shield current from (11) and (12), the matrix equation (9) can be minimized as (13) is shown at the bottom of this page where the shield effects are integrated into the new matrix of effective transmitter and receiver components. The effective inductance and resistance of the transmitter and receiver pad Z'_{11} and Z'_{44} and the effecive mutual inductance M'_{14} with the shield can be given as

$$M'_{14} = M_{14} + \frac{j\omega M_{12} M_{24}}{Z_{22}} + \frac{j\omega M_{13} M_{34}}{Z_{33}} \tag{14}$$

$$Z'_{11} = Z_{11} + \frac{\omega^2 M_{12}^2}{Z_{22}} + \frac{\omega^2 M_{13}^2}{Z_{33}} \tag{15}$$

$$Z'_{44} = Z_{44} + \frac{\omega^2 M_{24}^2}{Z_{22}} + \frac{\omega^2 M_{34}^2}{Z_{33}}. \tag{16}$$

Equations (15) and (16) show the modified effective impedance and mutual inductance of the coupled pads with shield compared to a shield-less system. From (10) and (15), Z'_{11} can be expressed as

$$\begin{aligned} Z'_{11} = &\left(R_1 + j\omega L_1 + \frac{1}{j\omega C_1}\right) + \frac{\omega^2 M_{12}^2}{|Z_{22}|^2}(R_2 + j\omega L_2) \\ &+ \frac{\omega^2 M_{13}^2}{|Z_{22}|^2}(R_3 + j\omega L_3) \end{aligned} \tag{17}$$

which can be further rearranged into effective resistive, inductive, and capacitive components as follows:

$$\begin{aligned} Z'_{11} = &\left(R_1 + \frac{\omega^2 M_{12}^2}{|Z_{22}|^2} R_2 + \frac{\omega^2 M_{13}^2}{|Z_{22}|^2} R_3\right) \\ &+ j\omega\left(L_1 - \frac{\omega^2 M_{12}^2}{|Z_{22}|^2} L_2 - \frac{\omega^2 M_{13}^2}{|Z_{22}|^2} L_3\right) + \frac{1}{j\omega C_1}. \end{aligned} \tag{18}$$

Here, the effect of the shield can be expressed as an effectively reduced inductance and increase series resistance of the primary coil (with core). The effective self-inductance of the transmitter with the shield can be as follows:

$$L'_1 = L_1 - L_2 \frac{\omega^2 M_{12}^2}{|Z_{22}|^2} - L_3 \frac{\omega^2 M_{13}^2}{|Z_{33}|^2}. \tag{19}$$

Similarly, from (10) and (16), the effective self-inductance of the receiver can be derived as

$$L'_4 = L_4 - L_2 \frac{\omega^2 M_{24}^2}{|Z_{22}|^2} - L_3 \frac{\omega^2 M_{34}^2}{|Z_{33}|^2}. \tag{20}$$

$$\begin{bmatrix} v_1 \\ 0 \end{bmatrix} = \begin{bmatrix} Z_{11} + \frac{\omega^2 M_{12}^2}{Z_{22}} + \frac{\omega^2 M_{13}^2}{Z_{33}} & -j\omega\left(M_{14} + \frac{j\omega M_{12} M_{24}}{Z_{22}} + \frac{j\omega M_{13} M_{34}}{Z_{33}}\right) \\ -j\omega\left(M_{14} + \frac{j\omega M_{12} M_{24}}{Z_{22}} + \frac{j\omega M_{13} M_{34}}{Z_{33}}\right) & Z_{44} + \frac{\omega^2 M_{24}^2}{Z_{22}} + \frac{\omega^2 M_{34}^2}{Z_{33}} \end{bmatrix} \begin{bmatrix} i_1 \\ i_4 \end{bmatrix} \tag{13}$$

In a typical WCS pad for EV application, the radius of the pad, hence the effective shield loop radius ranges from 100 to 300 mm and the consequent shield inductance ranges from 1 to 2 μH and the shield resistance is few tens of milliohms for an operating frequency of 20–100 kHz. In this range, $\omega L_2 \gg R_2$ and $\omega L_3 \gg R_3$. Hence, from (10), (17), and (18), the effective self-inductances L'_1 and L'_2 can be further simplified as follows:

$$L'_1 = L_1(1 - k_{12}^2 - k_{13}^2)$$
$$L'_4 = L_4(1 - k_{24}^2 - k_{34}^2). \tag{21}$$

Similarly, with the same assumptions of $\omega L_2 \gg R_2$ and $\omega L_3 \gg R_3$, the expression of the mutual inductance from (14) can be simplified as

$$M'_{14} = M_{14} + \frac{j\omega M_{12} M_{24}}{j\omega L_2} + \frac{j\omega M_{13} M_{34}}{j\omega L_3}. \tag{22}$$

Each of the shields is negatively coupled with its coil, and the mutual inductances can also be expressed as $M_{12} = k_{12}\sqrt{L_1 L_2}$, $M_{24} = k_{24}\sqrt{L_2 L_4}$, $M_{13} = k_{13}\sqrt{L_1 L_3}$, and $M_{34} = k_{34}\sqrt{L_3 L_4}$ and $M_{14} = k_{14}\sqrt{L_1 L_4}$. Using these expressions, the effective mutual inductance and the consequent coupling coefficient between the transmitter and receiver can be derived from (14) as

$$M'_{14} = M_{14}\left(1 - \frac{|k_{12}k_{24}|}{k_{14}} - \frac{|k_{13}k_{34}|}{k_{14}}\right) \tag{23}$$

$$k'_{14} = k_{14} - |k_{12}k_{24}| - |k_{13}k_{34}|. \tag{24}$$

It is evident that the shield reduces both the self- and mutual inductance of the shield, and (18)–(20) shows that this reduction can be calculated analytically and verified through FEA.

D. EMF Emission Suppression

The effective EMF leakage depends on the coil currents and the induced shield currents. The shield current increases linearly with the coil current for a fixed shield geometry. Consequently, the resultant EMF at any observation point also varies linearly. It was shown previously in Fig. 4(b) that under misalignment the flux density at the observation point, $B_{P\Delta}$ goes above the limit of 27 μT for more than 5-kW output power. Therefore, for higher power, the shield currents need to be increased to suppress the EMF below the ICNIRP limit. However, at high frequency, increasing the shield thickness or using low resistivity copper shield has an insignificant effect on increasing shield current. The design-level controllability of shield current with shield resistance and the shield-to-coil coupling coefficient is shown in Fig. 8. It indicates that the higher conductive copper shield or thicker aluminum does not effectively increase the shield current. However, the shield current is a strong function of the shield inductance and shield-to-coil coupling coefficients. Therefore, to achieve a certain shield current to suppress EMF emission, the effective coupling coefficient between the coil and its lumped shield needs to be attained through an appropriate shield design.

The shield is effectively a single-loop inductor and it is not convenient to design and optimize the shield inductance.

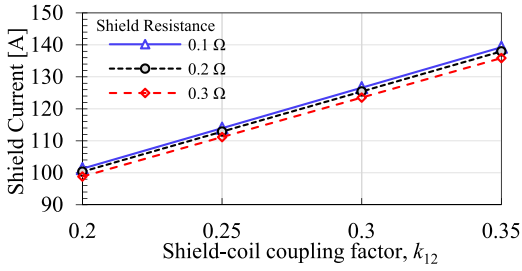

Fig. 8. Variation of the induced total shield current for the variation of shield-to-coil coupling k_{12} and shield resistance.

The shield inductance depends on the shield radius and its effective current carrying cross-sectional area as shown in (1). However, the effective coupling of the shield with the main coil can be designed and varied by optimizing the geometry of the outer edge of the shield. Therefore, the shield-to-coil coupling is one of the key design parameters to achieve the target shield current and suppress the EMF emission.

The shield current in the high-power applications which are more prone to exceeding the leakage field limit needs to be increased by increasing the shield-to-coil coupling. It can be achieved by increasing the height of the shield ring (SR), which eventually intersects with more flux emitting the core. On the other hand, the shield current in the low-power applications needs to be reduced, where the leakage flux is much lower than the ICNIRP limit. This reduction can be achieved by increasing the air gap between the core and the aluminum back plate of the pad. As this air gap increases, the mutual inductance M_{12} and M_{34} decreases; hence, the resultant induced current also decreases. Therefore, this air gap has been identified as a design parameter for low-leakage applications, while the SR height needs to be designed for high-leakage applications, where the shield current needs to be increased above a certain level to limit the leakage field below the safety level. In this paper, the design and optimization of the shield are done focusing on high-power applications and a detail optimization of shield right is presented in Section IV.

E. Shield Loss Reduction

Because the current in this shield of a WCS is highly localized around its outer boundary, the consequent loss can be reduced significantly by optimizing the outer edge of the shield. The magnitude of this shield current and consequent shield loss also depends on the flux density at the outer boundary of the core, which is determined by the core thickness. However, as the design of the core thickness is primarily dominated by core loss at a certain power, in this paper, the shield design is evaluated for a fixed core thickness.

The shield loss is proportional to the effective resistance of the shield current path. Therefore, the effective resistance of the shield current path around the core periphery needs to be reduced by increasing the effective conducting cross-sectional area of the shield current or increasing its conductivity. As discussed in Section III-B, copper has 21% higher ac conductivity than aluminum; however, it is approximately 3.1 times costlier

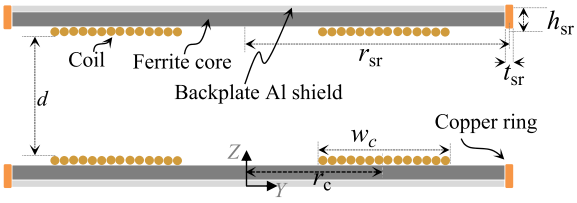

Fig. 9. Proposed hybrid shield structure with thinner aluminum plate and a copper shield ring (cross-sectional view on *YZ* plane).

TABLE II
FEA DESIGN SPECIFICATIONS

Parameter	Nominal value
Coil turn	$N_{tx} = N_{rx} = 14$
Coil outer radius, r_{co}	250 mm
Air-gap, d	150 mm
Ferrite core thickness	5 mm
Aluminum shield thickness	3.17 mm
Aluminum shield radius	300 mm

and 3.3 times heavier than aluminum. Therefore, fully replacing the aluminum shield by copper shield is not cost effective or mechanically preferable. Rather, the conductivity can be enhanced by only using a thin copper ring around the outer boundary of the traditional aluminum shield. Thereby, the overall shield resistance can be reduced significantly with a minimum increase in cost and weight. The details of this SR and consequent shield loss reduction is discussed in Section IV-A.

IV. SHIELD OPTIMIZATION

The major two objectives of the shield optimization are suppressing the EMF leakage under the ICNIRP limit and minimizing the shield loss. To achieve these goals, a low resistance shield structure is required which can be optimized to achieve the desired shield current to suppress the EMF below limit, considering both the electromagnetic and mechanical constraints of the charging pad. In Section III-C, the magnetic field suppressing shield current has been expressed in (11) and (12), showing it controllability by controlling the shield-to-coil mutual inductances. The characteristics of the shield loss shown in Fig. 6(c) and modeled into equivalent shield resistance (5), indicating that, only increasing the conductivity of the peripheral region of the shield, the loss can be reduced significantly. Based on these findings, a hybrid shield model has been proposed, which can be designed for different shielding efficacy at a reduced loss.

A. Proposed Shield Model

A hybrid shield structure is shown in Fig. 9, and the initial design parameters are given in Table II. In the proposed design, a thin copper SR is placed around the traditional aluminum shield. Depending on the size and position of the SR, the current induced in the SR can be more than 80% of the total shield current. Therefore, by altering only the outer edge of the shield with a copper SR, the loss-per-unit shield current can be reduced by 21% compared to the loss in an aluminum

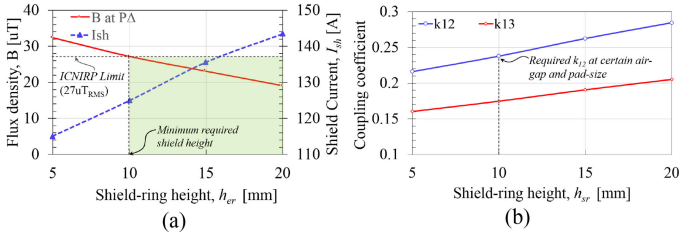

Fig. 10. Variation of the shield current and flux density, $B_{P\Delta}$ indicating minimum required SR height, and (b) variation of shield-to-coil couplings with the change of SR height.

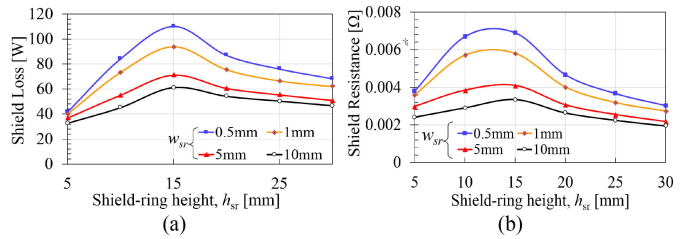

Fig. 11. Variation of (a) shield current and (b) shield equivalent resistance with the height and width variation of the SR.

TABLE III
PARAMETERS AND CONSTRAINTS OF OPTIMIZATION

Parameter	Constraint
Coupling coefficient	$k_{14} > k_{th} = 0.25$
Shield-ring loop radius	$r_{sr} \leq r_o = 300$ mm
End ring height	$2\sigma \leq h_{sr} \leq t_{pad} = 15$ mm
Shield-ring width	$t_{sr} \geq 2\delta_{copper} = 0.446$ mm
Aluminum shield thickness	$t_{Al} \geq t_{Al\text{-}min} = 0.5$ mm
Shield current	$I_{sh} \geq I_{sh\ th} = 125$ A
Flux density	$B_P < B_{th} = 27\ \mu$T

shield. The height, thickness, and the loop radius of the SR are the main optimization parameters to achieve the target shield-to-coil coupling required for a certain system with minimum shield loss.

B. Scope of Optimization

The shield-to-coil coupling with the variation of SR height, and the resulting shield current and consequent flux density at observation point P_Δ are shown in Fig. 10(a) and (b). Fig. 11 shows that the shield height has a significant effect on the shield current and equivalent shield resistance. It indicates that, for a certain coil current, a minimum SR height is required to suppress the EMF emission below the ICNIRP limit. On the other hand, the shield resistance decreases above a certain height of SR as shown in Fig. 11(b). However, the shield height is constrained by the pad thickness and can be increased up to a limited extent.

C. Algorithm and Constraints

The optimization constraints are set by the electromagnetic properties of the copper, ferrite, and aluminum, and the geometrical constraints are set by the size and thickness of the pad, as summarized in Table III. The maximum sizes of the shield

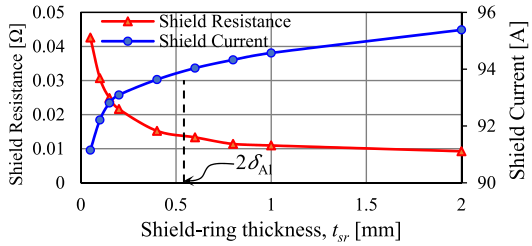

Fig. 12. Variation of shield current and loss with the thickness variation aluminum SR, showing a significantly increasing loss for the thickness lower than $2\delta_{A1}$.

TABLE IV
SETS OF SR PARAMETERS FOR OPTIMIZATION

Parameter set	Target variables	Design Parameter
p	SR inductance, coupling, position	h_{sr}, r_{sr}, z_{sr}
q	Resistivity and the current distribution	ρ_{sr}, A_{sr}

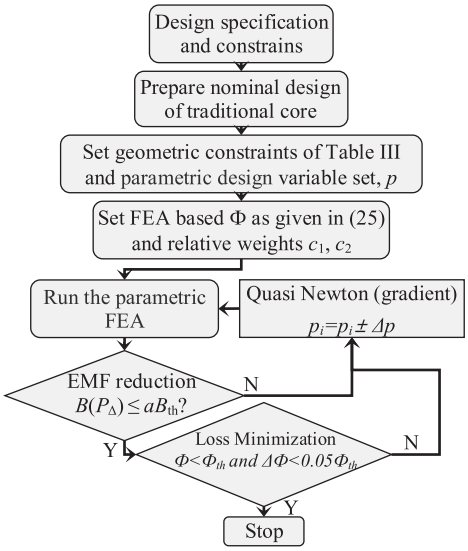

Fig. 13. Flowchart of the proposed optimization algorithm to suppress the EMF emission and minimize shield loss.

geometry are set by the maximum permitted radius and thickness of the pad, and the minimum thickness is constrained by twice the skin depth of the shield material.

Fig. 12 shows that, below this thickness, the effective resistivity of shield increases significantly, causing much higher loss. The geometric optimization parameters to limit the EMF and to reduce shield loss are given in Table IV. Here, p is the set of parameters that have strong effects on the EMF, and q is the parameter set that affects the shield resistance and consequent loss. The flowchart of the proposed optimization algorithm is shown in Fig. 13, where the main goal is limiting EMF emission by optimizing p and minimizing the shield loss by optimizing q.

Equation (25) shows the objective function Φ to minimize the shield loss and suppress the EMF below the threshold value

$$\Phi = c_1 \frac{P_{sh-op}}{P_{sh-Al}} + c_2 \frac{B}{B_{th}} f(B - aB_{th}) \tag{25}$$

TABLE V
OPTIMIZED SHIELD FOR A 7-kW SYSTEM

Parameter	Value
Effective coupling coefficient, k_{14}	0.28
Shield-ring loop radius	300 mm
End ring height	10.8 mm
Shield-ring width	0.8 mm
Aluminum shield thickness	0.9 mm

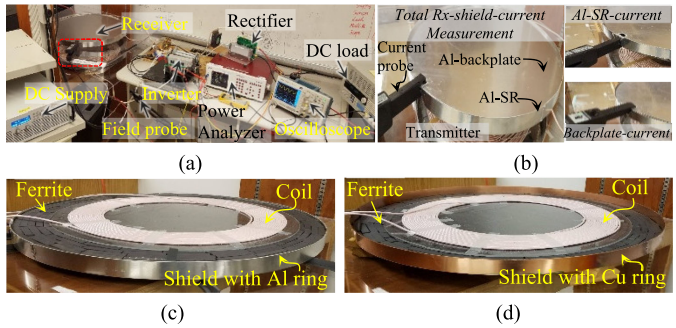

Fig. 14. (a) Experimental setup for a 7-kW vehicular WCS. (b) Setups for measuring currents in the back plate and shield ring, and the installation of pad with (c) aluminum SR and (d) copper SR.

where c_1 and c_2 are the relative weighting factors imposed on the shield loss reduction and EMF emission suppression; hence, $c_1 + c_2 = 1$. $P_{\mathrm{sh-Al}}$ and $P_{\mathrm{sh-op}}$ are the shield loss in the initial aluminum shield and proposed hybrid shield under optimization, and B_{th} is the maximum threshold flux density at P_{Δ}, which is 27 μT_{rms} set by the ICNIRP 2010 standard. The function f is defined as

$$f(B - aB_{th}) = \begin{cases} 1, & \text{if } B \geq aB_{\mathrm{th}} \\ 0, & \text{otherwise} \end{cases} \tag{26}$$

where a is a constant which can be used to impose an additional restriction on flux density limit during the design; therefore, $a \leq 1$. In this system, the maximum allowed flux density is set to the ICNIRP threshold of 27 μT; hence, $a = 1$. The relative weights, $c_{1,}$ and c_2, need to be defined based on application requirement. Therefore, if the ICNIRP limit is satisfied at the observation point, the value of the objective function Φ ranges between 0 and c_1, which is subject to minimize by optimizing geometry and minimizing the shield loss. Based on the theoretical analysis and through several FEA-based optimizations, it is observed that the shield loss can be reduced by more than 20% compared to the traditional aluminum shield; hence, the maximum value of the objective function is set as $\Phi_{\mathrm{th}} = 0.8c_1$. In this system, the EMF suppression and shield loss reduction are given the same emphasis; therefore, weights are set as $c_1 = 0.5$ and $c_2 = 0.5$. The subsequent result of the optimization is given in Table V.

V. EXPERIMENTAL SETUP AND RESULTS

A laboratory prototype of a 7-kW WCS is used to evaluate the proposed shielding which is shown in Fig. 14(a). Both the primary and secondary coils of the system are of a planar spiral

TABLE VI
EXPERIMENTAL PARAMETER OF CIRCULAR PAD

Parameter	Transmitter	Receiver
Number of turns	14	14
Self-inductance	196.6 μH	198.2 μH
Coupling coefficient	0.28	
Air-gap, d	150 mm	
SR inductance	1.42 μH	1.35 μH
Ferrite core thickness	5 mm	5 mm
Shield plate thickness	1.27 mm	1.27 mm
Shield-ring radius	303 mm	303 mm
Shield-ring height	10 mm	10 mm

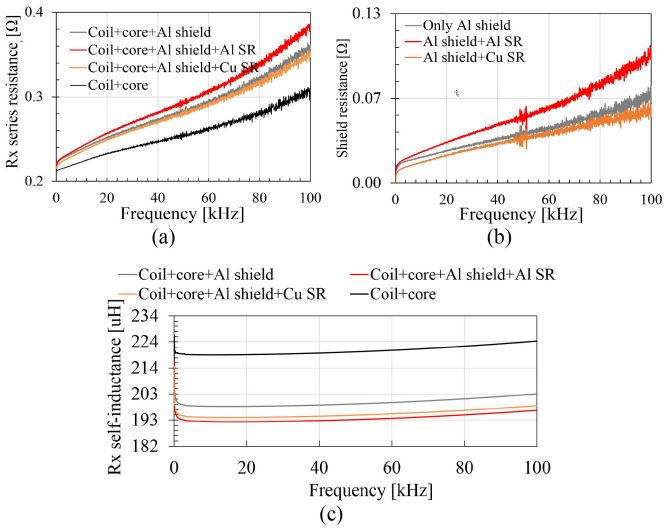

Fig. 15. (a) Series resistance comparison for different shield configurations. (b) Effective shield resistance for Al plate, Al-SR, and Cu-SR. (c) Reduction of the effective inductance of receiver under different shielding.

shape and made of 14 turns of AWG38x800 Litz wire. The core is made with ferrite tiles of three different sizes, BLK100/100/5-3C95: 100 mm × 100 mm × 5 mm, FR46410IC: 64 mm × 50 mm × 5 mm, FR45810IC: 58 mm × 38 mm × 4 mm, FR43208IC: 32 mm × 20 mm × 3.2 mm. The transmitter and receiver shields are made with high conductivity aluminum 6101 alloy sheet with an electrical conductivity of 49.9% in the scale of International Annealed Copper Standard [25]. Two different shield thicknesses have been evaluated: 1.27 and 3.17 mm to observe the variation of the shield resistance with the shield thickness.

To evaluate the EMF suppression and loss comparison, both the aluminum and copper SR are tested with an aluminum back plate as shown in Fig. 14(b) and (c). Moreover, an open terminal SR is used to evaluate the shield inductance and shield-to-coil coupling. The system parameters of the experimental setup are given in Table VI. The effective resistance of the coil and shield is measured with a network analyzer (BODE 100) with high precision B-WIC adapter as shown in Fig. 14(a).

The additional shield resistance is shown in Fig. 15(a), which indicates the difference in series resistance of transmitter pad with aluminum and copper SR. The comparative effective shield resistance of the aluminum plate, the aluminum plate with aluminum SR, and the aluminum plate with copper SR are shown

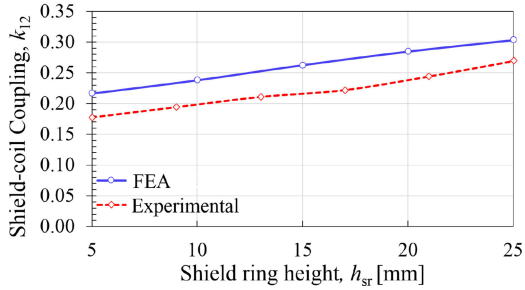

Fig. 16. Variation of coil-to-shield coupling of the transmitter pad with the variation of height of the SR.

in Fig. 15(b). Compared to the "coil + core + Al shield plate" configuration, the shield current and consequent shielding effectiveness for the "coil + core + Al shield plate + Al/Cu SR" is higher due to its higher coupling with the coils. Consequently, the induced shield current and the shield loss in it are also higher than Al plate, as indicated in Fig. 15(a).

When the Al-SR is replaced by the Cu-SR, the shield loss has been reduced while maintaining the same shielding effectiveness. The reduction in the shield loss is reflected through the reduction in high frequency (85 kHz) shield resistance in the system with copper-SR (48 mΩ), compared to the system with aluminum-SR (85 mΩ), as shown in Fig. 15(b). The reduction of the effective pad inductance with a shield depends on the coupling among the coils and the shields, as derived in (18); this is experimentally verified for all four configurations of receiver pad as shown in Fig. 15(c). With the addition of the SR, together with the shield plate, the coil-to-shield coupling increases, which increase the shielding efficacy while reducing the effective pad inductance.

The coil-to-shield coupling coefficient is evaluated with the ring height variation, as shown in Fig. 16. The results show that the shield–coil coupling can be increased up to 51% as the SR height is limited by the maximum allowed pad thickness. This increased coil-to-shield coupling corresponds to a 24.5% increase in shield current, providing greater design flexibility for shielding to that limits the EMF. It also indicates that using the SR for mechanical stability or increasing the height of the SR at low power, where the magnetic field is typically much lower than the ICNIRP limit, causes higher shield current and additional loss. Therefore, the SR has to be used only for high-power application where the magnetic field is susceptible to exceed the safety limit.

The shield current was found highly localized around the outer boundary of the core through the FEA simulation as shown in Fig. 6. Therefore, a hole was created in the shield plate near its outer edge and a notch was created on the upper side of the SR to put a Hall effect-based current probe and measure the shield current. This setting allowed us to measure the shield current in the shield plate and ring separately and simultaneously. The shield current was measured by a Hall effect-based Tektronix Current Probe (A622), as shown in Fig. 14(b). It has a dc to 100-kHz frequency range and a "long nose" type narrow core making it suitable for this measurement in a compact setting. Three inset figures in Fig. 14(b) show the measurement of total

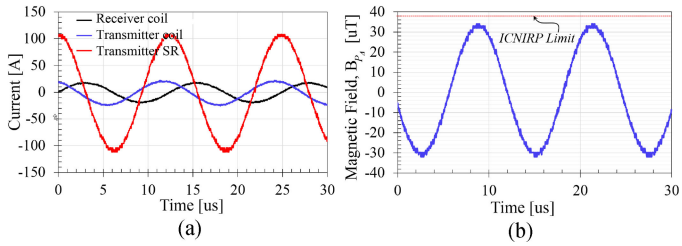

Fig. 17. (a) Current in the transmitter and receiver coils and corresponding SR current. (b) Consequent magnetic field at the observation point P_Δ (600 mm from the center of Tx).

shield current measurement, Al back plate current measurement, and the Al-SR current measurement separately for the shield configurations with Al back plate and Al-SR. The measured current in the coils and corresponding induced current in the transmitter SR are shown in Fig. 17(a). It shows that a total 105-A peak current is induced in the SR, and 18-A peak current is induced at the shield plate edge, measured directly using current probes. The result verifies that the shield current is highly localized at the outer boundary and SR, validating the proposed model in Section III-A.

The magnetic field density at the observation point is measured using an MC162 magnetic sensor, which can be directly connected with the oscilloscope. This magnetic field sensor is suitable for 2 kHz 1 MHz providing an output voltage of 10 mV per micro-Tesla field. However, as it is a single-axis magnetic field probe, the orientation of the probe is crucially important. At the observation point, the normalized ratio of the magnetic field vector from the circular coil-based WCS along the *X*-, *Y*-, and *Z*-axis are approximately 2:4:94, which was verified both through simulation and experiment. Therefore, the probe was aligned along each direction to measure each component of the field. The resultant magnetic field at P_Δ is shown in Fig. 17(b), which confirm the root-mean-square (rms) value of magnetic field density at observation point P_Δ is effectively suppressed to 24.8 μT, which is below the ICNIRP limit of 27 μT.

The resonant frequency of the transmitter and receiver coil was found varying between 88 and 93 kHz due to the variation of the effective self-inductance under different shielding configurations. Therefore, one of the main challenges of comparing the shield loss of different shield configurations was that due to this variation of effective self-inductance the resonance frequency of the system changes. Therefore, if the inverter is operated at the same switching frequency, which is mandatory to keep the loss in the core and coil same, the performance and efficiency of the inverter change. This happens due to the variation of the relative phase in the inverter current and voltage with the variation of the difference between the switching frequency and the resonance frequency. However, at a fixed switching frequency, the performance of the compensation capacitance and the passive rectifier does not change. Therefore, using the power analyzer, the input power of the resonant tank can be measured and using the digital-dc load the output dc power can be measured. From this result, the relative increase and reduction of the shield loss can be calculated from the comparison of the resonant tank's input to dc-load efficiency.

To achieve the zero-voltage switching and to avoid the sensitivity of the coil, core and shield loss with frequency, the inverter is operated at the fixed 100-kHz frequency for all three shield configurations. The inverter output power is measured by a single-phase power analyzer (PPA4510) and the output power from the digital dc load. The Al back plate shield without any SR showed the peak inverter output to dc-load efficiency of 91.78%. However, as the Al shield ring is added, the peak efficiency decreases to 90.7% and the resonance frequency increases. This shield loss with the Al-SR increases due to increased current in the shield, which makes the shielding more effective to suppress the leakage magnetic field. Replacing only the Al-SR by the proposed CU-SR, the peak 92.09% efficiency is achieved, reducing the loss while maintaining the same shielding effectiveness. Except for the shield configuration, all other components of the pad were kept unchanged to distinguish and compare the loss of different shield configurations. The resultant shield loss in the "Al plate + Al-SR" was found increased by 75 W compared to the Al plate shield. Finally, the shield loss in the "Al plate + Cu-SR" was found reduced by 97 W compared to the similar "Al plate + Al-SR" shield, while both have the same shielding effectiveness. Although the traditional Al back plate shield showed a high efficiency, the proposed shielding with Al plate and Cu-SR demonstrated higher efficiency as well as higher shielding effectiveness keeping the leakage flux density below the ICNIRP limit, which was the primary focus of the shield optimization.

VI. Conclusion

In this paper, the suppression of EMF emission in the WCS by a conductive shield is modeled for a circular pad WCS. From the developed lumped model, the shield current characteristics are studied together with the FEA. The EMF emission and shield loss characteristics for different shield parameters are investigated. Finally, a hybrid shield consisting of a thin aluminum plate with copper shield ring is proposed as a low loss cost-effective alternative to the traditional aluminum shield. The experimental result shows that up to 24.5% higher shield current can be induced in the optimized hybrid shield by varying the SR height. The experimental result shows that while suppressing the EMF below ICNIRP limit, the shield loss in the proposed shied with Cu-SR has been reduced by 15.98% as compared to the equivalent shield with Al-SR.

References

[1] B. Choi, J. Nho, H. Cha, T. Ahn, and S. Choi, "Design and implementation of low-profile contactless battery charger using planar printed circuit board windings as energy transfer device," *IEEE Trans. Ind. Electron.*, vol. 51, no. 1, pp. 140–147, Feb. 2004.

[2] Y. Jang and M. M. Jovanovic, "A contactless electrical energy transmission system for portable-telephone battery chargers," *IEEE Trans. Ind. Electron.*, vol. 50, no. 3, pp. 520–527, Jun. 2003.

[3] A. W. Green and J. T. Boys, "10 kHz inductively coupled power transfer-concept and control," in *Proc. 5th Int. Conf. Power Electron. Variable-Speed Drives*, Oct. 1994, pp. 694–699.

[4] G. A. Covic and J. T. Boys, "Modern trends in inductive power transfer for transportation applications," *IEEE J. Emerg. Sel. Topics Power Electron.*, vol. 1, no. 1, pp. 28–41, Mar. 2013.

[5] Z. Luo and X. Wei, "Analysis of square and circular planar spiral coils in wireless power transfer system for electric vehicles," *IEEE Trans. Ind. Electron.*, vol. 65, no. 1, pp. 331–341, Jan. 2018.

[6] M. Mohammad, S. Choi, Z. Islam, S. Kwak, and J. Baek, "Core design and optimization for better misalignment tolerance and higher range of wireless charging of PHEV," *IEEE Trans. Transp. Electrific.*, vol. 3, no. 2, pp. 445–453, Jun. 2017.
[7] S. Y. R. Hui, W. Zhong, and C. K. Lee, "A critical review of recent progress in mid-range wireless power transfer," *IEEE Trans. Power Electron.*, vol. 29, no. 9, pp. 4500–4511, Sep. 2014.
[8] P. P. Ding, L. Bernard, L. Pichon, and A. Razek, "Evaluation of electromagnetic fields in human body exposed to wireless inductive charging system," *IEEE Trans. Magn.*, vol. 50, no. 2, pp. 1037–1040, Feb. 2014.
[9] *Guidelines for Limiting Exposure to Time-Varying Electric and Magnetic Fields (1 Hz to 100 kHz)*, Neuherberg, Germany, 2010.
[10] L. Percebon and D. Kuerschner, "Magnetic leakage azimuth pattern of a 7 kW wireless electric charging system in different environments," in *Proc. PCIM Eur. Int. Exhib. Conf. Power Electron. Intell. Motion Renewable Energy Energy Manage.*, May 2017, pp. 1–8.
[11] A. Tejeda, C. Carretero, J. T. Boys, and G. A. Covic, "Ferrite-less circular pad with controlled flux cancelation for EV wireless charging," *IEEE Trans. Power Electron.*, vol. 32, no. 11, pp. 8349–8359, Nov. 2017.
[12] F. Y. Lin, G. A. Covic, and J. T. Boys, "Leakage flux control of mismatched IPT systems," *IEEE Trans. Transp. Electrific.*, vol. 3, no. 2, pp. 474–487, Jun. 2017.
[13] R. Pinto *et al.*, "Exposure assessment of stray electromagnetic fields generated by a wireless power transfer system," in *Proc. 9th Eur. Conf. Antennas Propag.*, May 2015, pp. 1–4.
[14] M. Jo, Y. Sato, Y. Kaneko, and S. Abe, "Methods for reducing leakage electric field of a wireless power transfer system for electric vehicles," in *Proc. IEEE Energy Convers. Congr. Expo.*, Sep. 2014, pp. 1762–1769.
[15] H. Kim, J. Cho, S. Ahn, J. Kim, and J. Kim, "Suppression of leakage magnetic field from a wireless power transfer system using ferrimagnetic material and metallic shielding," in *Proc. IEEE Int. Symp. Electromagn. Compat.*, Aug. 2012, pp. 640–645.
[16] H. Kim *et al.*, "Design of magnetic shielding for reduction of magnetic near field from wireless power transfer system for electric vehicle," in *Proc. Int. Symp. Electromagn. Compat.*, Sep. 2014, pp. 53–58.
[17] F. Y. Lin, A. Zaheer, M. Budhia, and G. A. Covic, "Reducing leakage flux in IPT systems by modifying pad ferrite structures," in *Proc. IEEE Energy Convers. Congr. Expo.*, Sep. 2014, pp. 1770–1777.
[18] S. Y. Choi, B. W. Gu, S. W. Lee, W. Y. Lee, J. Huh, and C. T. Rim, "Generalized active EMF cancel methods for wireless electric vehicles," *IEEE Trans. Power Electron.*, vol. 29, no. 11, pp. 5770–5783, Nov. 2014.
[19] S. Ahn and J. Kim, "Magnetic field design for high efficient and low EMF wireless power transfer in on-line electric vehicle," in *Proc. 5th Eur. Conf. Antennas Propag.*, Apr. 2011, pp. 3979–3982.
[20] P. R. Bannister, "New theoretical expressions for predicting shielding effectiveness for the plane shield case," *IEEE Trans. Electromagn. Compat.*, vol. EMC-10, no. 1, pp. 2–7, Mar. 1968.
[21] Y. Du, T. C. Cheng, and A. S. Farag, "Principles of power-frequency magnetic field shielding with flat sheets in a source of long conductors," *IEEE Trans. Electromagn. Compat.*, vol. 38, no. 3, pp. 450–459, Aug. 1996.
[22] S. Kim, H. H. Park, J. Kim, J. Kim, and S. Ahn, "Design and analysis of a resonant reactive shield for a wireless power electric vehicle," *IEEE Trans. Microw. Theory Techn.*, vol. 62, no. 4, pp. 1057–1066, Apr. 2014.
[23] Y. Yashima, H. Omori, T. Morizane, N. Kimura, and M. Nakaoka, "Leakage magnetic field reduction from wireless power transfer system embedding new eddy current-based shielding method," in *Proc. Int. Conf. Elect. Drives Power Electron.*, Sep. 2015, pp. 241–245.
[24] *Task Force on Wireless Power Charging*, SAE J2954. [Online]. Available: http://www.sae.org. Accessed on: May 5, 2018.
[25] Z. Pakiela, K. Ludwichowska, J. Ferenc, and M. Kulczyk, "Mechanical properties and electrical conductivity of Al6101 and 6201 alloys processed by hydro-extrusion," in *Proc. IOP Conf. Ser. Mater. Sci. Eng.*, vol. 63, 2014, no. 1, Art. no. 012120.
[26] *C-95 Material Specification*. Ferroxcube. [Online]. Available: https://www.ferroxcube.com. Accessed on: Dec. 3, 2017.
[27] R. Dengler, "Self inductance of a wire loop as a curve integral," *Adv. Electromagn.*, vol. 5, no. 1, pp. 1–8, Jan. 2016.
[28] E. B. Rosa and W. Grover Frederick, "Formulas and tables for the calculation of mutual and self-inductance," NBS Sci. Paper no. 169, 3rd ed., Dec. 1916, pp. 110–111.
[29] N. Ida, *Engineering Electromagnetics*, 2nd ed. New York, NY, USA: Springer Sci. Bus. Media, 2007, p. 774.
[30] *Magnetic Sciences, Magnetic Sensors for 5 Hz–1 MHz*. [Online]. Available: http://www.magneticsciences.com. Accessed on: Dec. 3, 2017.
[31] M. Mohammad, M. S. Haque, and S. Choi, "A Litz-wire based passive shield design to limit EMF emission from wireless charging system," in *Proc. IEEE Energy Convers. Congr. Expo.*, Portland, OR, USA, Sep. 2018, pp. 97–104.

Mostak Mohammad (S'15) received the B.Sc. degree in electrical and electronic engineering from the Bangladesh University of Engineering and Technology, Dhaka, Bangladesh, in 2009, and has been working toward the Ph.D. degree in electrical engineering at the University of Akron, Akron, OH, USA, since 2014.

From 2009 to 2014, he was a Radio Network Specialist with Robi Axiata Limited, Dhaka. His current research interests include high-power wireless charging system for electric vehicles, high-frequency magnetics, and high-frequency power converter.

Eshet Tezera Wodajo (S'19) received the B.Sc. degree in electrical engineering from Addis Ababa University, Addis Ababa, Ethiopia, in 2013, and is currently working toward the Ph.D. degree at the University of Akron, Akron, OH, USA.

He was a Junior Electrical Engineer with Ethiopian Airports Enterprise from 2013 to 2014, and an Assistant Lecturer with Addis Ababa University from 2014 to 2016. His research interests include power electronics, drive mechanism, renewable energy systems, and control systems.

Seungdeog Choi (S'07–M'12–SM'16) received the B.S. degree from Chung-Ang University, Seoul, South Korea, in 2004, the M.S. degree from Seoul National University, Seoul, in 2006, and the Ph.D. degree in electric power and power electronics program from Texas A&M University, College Station, TX, USA, in 2010.

From 2006 to 2007, he was a Research Engineer with LG Electronics, Seoul. From 2009 to 2012, he was a Research Engineer with Toshiba International Corporation, Houston, TX, USA. He was an Assistant Professor with the University of Akron, Akron, OH, USA, from 2012 to 2018. He has been an Associate Professor with Mississippi State University, Starkville, MS, USA, since 2018. His current research interests include the degradation modeling, fault-tolerant controls, fault-tolerant design, and electromagnetic interference analysis of electric machines, power electronics systems in the applications of transportation electrification, microgrid, and smart grid systems.

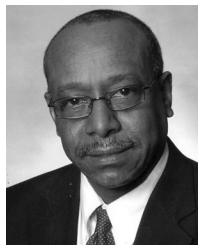

Malik E. Elbuluk (S'79–M'79–SM'97) received the B.Sc. (Hons.) degree from the University of Khartoum, Khartoum, Sudan, in 1976, and the M.S., E.E., and D.Sc. degrees from the Massachusetts Institute of Technology, Cambridge, MA, USA, in 1980, 1981, and 1986, respectively, all in electrical engineering.

He has been a Professor with the University of Akron, Akron, OH, USA, since 1989. He was with the Faculty of the Department of Electrical and Computer Engineering and the Electric Power Research Center, North Carolina State University, from 1986 to 1989. He was a Summer Research Fellow with NASA Lewis Research Center, Cleveland, OH, USA, from 1991 to 2014. His work at NASA included low-temperature electronics for space missions, modeling and simulation of the Space Station Freedom, the power by wire, the power electronic building blocks, and the starter/generator for aircraft engines and sensorless control of electromechanical actuators for the more electric aircraft. His teaching and research interests include the areas of power electronics, electric machines, control systems, fuzzy logic, and neural networks.

Dr. Elbuluk actively publishes and reviews papers for IEEE Conferences and Transactions, and has organized and chaired a number of sessions for the Power Electronics, the Industry Application, and the Industrial Electronics Societies. He was an Associate Editor for the IEEE TRANSACTIONS ON POWER ELECTRONICS and is currently the Manufacturing Systems Development and Applications Department Vice President for the IEEE TRANSACTIONS ON INDUSTRY APPLICATIONS and also the Vice President and Technical Program Chair for the Industry Automation and Control Committee. He is a registered Professional Engineer in Ohio.